

# Deep Discriminative to Kernel Density Graph for In- and Out-of-distribution Calibrated Inference

Jayanta Dey,<sup>1,\*</sup> Will LeVine,<sup>1,2</sup> Ashwin De Silva,<sup>1,†</sup> Haoyin Xu,<sup>1,†</sup> Tyler M. Tomita,<sup>1</sup> Ali Geisa,<sup>1</sup>  
Jacob Desman,<sup>1</sup> and Joshua T. Vogelstein<sup>1</sup>

**Abstract.** Deep discriminative approaches like random forests and deep neural networks have recently found applications in many important real-world scenarios. However, deploying these learning algorithms in safety-critical applications raises concerns, particularly when it comes to ensuring confidence calibration for both in-distribution and out-of-distribution data points. Many popular methods for in-distribution (ID) calibration, such as isotonic and Platt's sigmoidal regression, exhibit excellent ID calibration performance. However, these methods are not calibrated for the entire feature space, leading to overconfidence in the case of out-of-distribution (OOD) samples. On the other end of the spectrum, existing out-of-distribution (OOD) calibration methods generally exhibit poor in-distribution (ID) calibration. In this paper, we address ID and OOD calibration problems jointly. We leveraged the fact that deep models, including both random forests and deep-nets, learn internal representations which are unions of polytopes with affine activation functions to conceptualize them both as partitioning rules of the feature space. We replace the affine function in each polytope populated by the training data with a Gaussian kernel. Our experiments on both tabular and vision benchmarks show that the proposed approaches obtain well-calibrated posteriors while mostly preserving or improving the classification accuracy of the original algorithm for in-distribution region, and extrapolate beyond the training data to handle out-of-distribution inputs appropriately.

**1 Introduction** Machine learning methods, specially deep neural networks and random forests have shown excellent performance in many real-world tasks, including drug discovery, autonomous driving and clinical surgery. However, calibrating confidence over the whole feature space for these approaches remains a key challenge in the field. Although these learning algorithms can achieve near optimal performance at inferring on the samples lying in the high density regions of the training data [1–3], they yield highly confident predictions for the samples lying far away from the training data [4]. Calibrated confidence within the training or in-distribution (ID) region as well as in the out-of-distribution (OOD) region is crucial for safety critical applications like autonomous driving and computer-assisted surgery, where any aberrant reading should be detected and taken care of immediately [4, 5]. A well-calibrated model capable of quantifying the uncertainty associated with inference for any points from the training distribution as well as detecting OOD data can be a life-saver in these cases.

The approaches to calibrate OOD confidence for learning algorithms described in the literature can be roughly divided into two groups: discriminative and generative. Intuitively, the easiest solution for OOD confidence calibration is to learn a function that gives higher scores for in-distribution samples and lower scores for OOD samples, and thereby re-scale the posterior or confidence score from the original model accordingly [6]. The discriminative approaches try to either modify the loss function [7–9] or train the network exhaustively on OOD datasets to calibrate on OOD samples [4, 10]. Recently, as shown by Hein et al. [4], the ReLU networks produce arbitrarily high confidence as the inference point moves far away from the training data. Therefore, calibrating ReLU networks for the whole OOD region is not possible without fundamentally changing the network architecture. As a result, all of the aforementioned algorithms are unable to provide any guarantee about the performance of the network throughout the whole feature space. The other group tries to learn generative models for the in-distribution as well as the out-of-distribution samples. The general idea is to conduct likelihood ratio tests for a particular sample using the generative models [11], or threshold the ID likelihoods to detect OOD samples. However, it is not obvious how to control likelihoods far away from the training data for powerful generative models like variational autoencoders (VAEs) [12] and generative adversarial networks (GAN) [13]. Moreover,

<sup>1</sup> Johns Hopkins University (JHU), <sup>2</sup>Scale AI

\* corresponding author: [jdey4@jhu.edu](mailto:jdey4@jhu.edu), † denotes equal contribution

Nalisnick et al. [14] and Hendrycks et al. [10] showed VAEs and GANs can also yield overconfident likelihoods far away from the training data.

The algorithms described so far are concerned with OOD confidence calibration for deep-nets only. However, in this paper, we show that other approaches which partition the feature space, for example random forest, can also suffer from poor confidence calibration both in the ID and the OOD regions. Moreover, the algorithms described above are concerned about the confidence in the OOD region only and do not address the confidence calibration within the in-distribution at all. This issue is addressed separately in a different group of literature [15–20]. Instead, we consider both calibration problems jointly and propose an approach that achieves good calibration throughout the whole feature space.

In this paper, we conceptualize both random forest and ReLU networks as partitioning rules with an affine activation over each polytope. We consider replacing the affine functions learned over the polytopes with Gaussian kernels. We propose two novel kernel density estimation techniques named *Kernel Density Forest* (KDF) and *Kernel Density Network* (KDN). Our proposed approach completely excludes the need for training on OOD examples for the model (unsupervised OOD calibration). We conduct several simulation and real data studies that show both KDF and KDN are well-calibrated for OOD samples while they maintain good performance in the ID region.

**2 Related Works and Our Contributions** There are a number of approaches in the literature which attempt to learn a generative model and control the likelihoods far away from the training data. For example, Ren et al. [11] employed likelihood ratio test for detecting OOD samples. Wan et al. [8] modified the training loss so that the downstream projected features follow a Gaussian distribution. However, there is no guarantee of performance for OOD detection for the above methods. To the best of our knowledge, apart from us, only Meinke et al. [5] has proposed an approach to guarantee asymptotic performance for OOD detection. They model the training and the OOD distribution using Gaussian mixture models which enable them to control the class conditional posteriors far away from the training points. Compared to the aforementioned methods, our approach differs in several ways:

- We address the confidence calibration problems for both ReLU-nets and random forests from a common ground.
- We address in-distribution (ID) and out-of-distribution (OOD) calibration problem as a continuum rather than two separate problems.
- We provide an algorithm for OOD confidence calibration for both tabular and vision datasets whereas most of the OOD calibration methods in the literature are tailor-made for vision problems.
- We propose an unsupervised OOD calibration approach, i.e., we do not need to train exhaustively on different OOD samples.

### 3 Technical Background

**3.1 Setting** Consider a supervised learning problem with independent and identically distributed training samples  $\{(\mathbf{x}_i, y_i)\}_{i=1}^n$  such that  $(\mathbf{X}, Y) \sim P_{X,Y}$ , where  $\mathbf{X} \sim P_X$  is a  $\mathcal{X} \subseteq \mathbb{R}^D$  valued input and  $Y \sim P_Y$  is a  $\mathcal{Y} = \{1, \dots, K\}$  valued class label. Let  $S$  be a high density region of the marginal,  $P_X$ , thus  $S \subseteq \mathcal{X}$ .

**Definition 1 (In- and Out-of-distribution Samples).** If  $\mathbf{x} \in S$ , it is an in-distribution (ID) sample and if  $\mathbf{x} \notin S$ , it is an out-of-distribution (OOD) sample.

Here the goal is to learn a confidence score,  $\mathbf{g} : \mathbb{R}^D \rightarrow [0, 1]^K$ ,  $\mathbf{g}(\mathbf{x}) = [g_1(\mathbf{x}), g_2(\mathbf{x}), \dots, g_K(\mathbf{x})]$  such that,

$$(1) \quad g_y(\mathbf{x}) = \begin{cases} P_{Y|X}(y|\mathbf{x}), & \text{if } \mathbf{x} \in S \\ P_Y(y), & \text{if } \mathbf{x} \notin S \end{cases}, \quad \forall y \in \mathcal{Y}$$

where  $P_{Y|X}(y|\mathbf{x})$  is the posterior probability for class  $y$  given by the Bayes formula:

$$(2) \quad P_{Y|X}(y|\mathbf{x}) = \frac{P_{X|Y}(\mathbf{x}|y)P_Y(y)}{\sum_{k=1}^K P_{X|Y}(\mathbf{x}|k)P_Y(k)}, \quad \forall y \in \mathcal{Y}.$$

Here  $P_{X|Y}(\mathbf{x}|y)$  is the class conditional density for the training data which we will refer as  $f_y(\mathbf{x})$  hereafter for brevity.

**3.2 Main Idea** Deep discriminative networks partition the feature space  $\mathbb{R}^d$  into a union of  $p$  affine polytopes  $Q_r$  such that  $\bigcup_{r=1}^p Q_r = \mathbb{R}^d$ , and learn an affine function over each polytope [4, 21]. Mathematically, the class-conditional density for the label  $y$  estimated by these deep discriminative models at a particular point  $\mathbf{x}$  can be expressed as:

$$(3) \quad \hat{f}_y(\mathbf{x}) = \sum_{r=1}^p (\mathbf{a}_r^\top \mathbf{x} + b_r) \mathbb{1}(\mathbf{x} \in Q_r).$$

For example, in the case of a decision tree,  $\mathbf{a}_r = \mathbf{0}$ , i.e., decision tree assumes uniform distribution for the class-conditional densities over the leaf nodes. Among these polytopes, the ones that lie on the boundary of the training data extend to the whole feature space and hence encompass all the OOD samples. Since the posterior probability for a class is determined by the affine activation over each of these polytopes, the algorithms tend to be overconfident when making predictions on the OOD inputs. Moreover, there exist some polytopes that are not populated with training data. These unpopulated polytopes serve to interpolate between the training sample points. If we replace the affine activation function of the populated polytopes with Gaussian kernels and prune the unpopulated ones, the tail of the kernel will help interpolate between the training sample points while assigning lower likelihood to the low density or unpopulated polytope regions of the feature space. This results in better confidence calibration for the proposed modified approach.

**3.3 Proposed Approach** We will call the above discriminative approaches as the ‘parent approach’ hereafter. Consider the collection of polytope indices  $\mathcal{P}$  from the parent approach which contains the indices of total  $\tilde{p}$  polytopes populated by the training data. We replace the affine functions over the populated polytopes with Gaussian kernels  $\mathcal{G}(\cdot; \hat{\mu}_r, \hat{\Sigma}_r)$ . For a particular inference point  $\mathbf{x}$ , we consider the Gaussian kernel with the minimum distance from the center of the kernel to the corresponding point:

$$(4) \quad r_{\mathbf{x}}^* = \underset{r}{\operatorname{argmin}} \|\mu_r - \mathbf{x}\|,$$

where  $\|\cdot\|$  denotes a distance. As we will show later, the type of distance metric considered in Equation 4 highly impacts the performance of the proposed model. In short, we modify Equation 3 from the parent ReLU-net or random forest to estimate the class-conditional density as:

$$(5) \quad \tilde{f}_y(\mathbf{x}) = \frac{1}{n_y} \sum_{r \in \mathcal{P}} n_{ry} \mathcal{G}(\mathbf{x}; \mu_r, \Sigma_r) \mathbb{1}(r = r_{\mathbf{x}}^*),$$

where  $n_y$  is the total number of samples with label  $y$  and  $n_{ry}$  is the number of samples from class  $y$  that end up in polytope  $Q_r$ . We add a small constant to the class conditional density  $\tilde{f}_y$ :

$$(6) \quad \hat{f}_y(\mathbf{x}) = \tilde{f}_y(\mathbf{x}) + \frac{b}{\log(n)}.$$

Note that in Equation 6,  $\frac{b}{\log(n)} \rightarrow 0$  as the total training points,  $n \rightarrow \infty$ . The intuition behind the added constant will be clarified further later in Proposition 4. The confidence score  $\hat{g}_y(\mathbf{x})$  for class  $y$  given a test point  $\mathbf{x}$  is estimated using the Bayes rule as:

$$(7) \quad \hat{g}_y(\mathbf{x}) = \frac{\hat{f}_y(\mathbf{x})\hat{P}_Y(y)}{\sum_{k=1}^K \hat{f}_k(\mathbf{x})\hat{P}_Y(k)},$$

where  $\hat{P}_Y(y)$  is the empirical prior probability of class  $y$  estimated from the training data. We estimate the class for a particular inference point  $\mathbf{x}$  as:

$$(8) \quad \hat{y} = \operatorname{argmax}_{y \in \mathcal{Y}} \hat{g}_y(\mathbf{x}).$$

**3.4 Desiderata** We desire our proposed model to estimate confidence score  $\hat{g}_y$  to satisfy the following three desiderata:

1. **Empirical Classification Accuracy** : For finite sample cases, our goal is to maintain or even enhance the parent approach's ID accuracy on standard benchmark datasets.
2. **Empirical ID Calibration** On standard benchmark datasets, we aim to enhance the ID calibration of the parent approach.
3. **Empirical OOD Calibration** We aim to enhance the OOD calibration of the parent approach against any OOD datasets.

We run extensive experiments on various simulation and benchmark datasets in Section 5 to empirically verify that our proposed approach achieves Desiderata 1, 2 and 3.

**4 Kernel Density Graph** In this section we describe how we estimate the parameters shown in Equation 5.

**4.1 Gaussian Kernel Parameter Estimation** We fit Gaussian kernel parameters to the samples that end up in the  $r$ -th polytope. We set the kernel center along a dimension  $d$  as:

$$(9) \quad \hat{\mu}_r^d = \frac{1}{n_r} \sum_{i=1}^n x_i^d \mathbb{1}(\mathbf{x}_i \in Q_r),$$

where  $x_i^d$  is the value of  $\mathbf{x}_i$  along the  $d$ -th dimension. We set the kernel variance along a dimension  $d$  as:

$$(10) \quad (\hat{\sigma}_r^d)^2 = \frac{1}{n_r} \left\{ \sum_{i=1}^n \mathbb{1}(\mathbf{x}_i \in Q_r) (x_i^d - \hat{\mu}_r^d)^2 + \lambda \right\},$$

where  $\lambda$  is a small constant that prevents  $\hat{\sigma}_r^d$  from being 0. We constrain our estimated Gaussian kernels to have diagonal covariance.

**4.2 Sample Size Ratio Estimation** For a high dimensional dataset with low training sample size, the polytopes are sparsely populated with training samples. For improving the estimate of the ratio  $\frac{n_{ry}}{n_y}$  in Equation 5, we incorporate the samples from other polytopes  $Q_s$  based on the similarity  $w_{rs}$  between  $Q_r$  and  $Q_s$  as:

$$(11) \quad \begin{aligned} \left( \frac{\hat{n}_{ry}}{n_y} \right) &= \frac{\tilde{w}_{ry}}{\tilde{w}_y} = \frac{\tilde{w}_{ry}}{\sum_{r \in \mathcal{P}} \tilde{w}_{ry}} \\ &= \frac{\sum_{s \in \mathcal{P}} \sum_{i=1}^n w_{rs} \mathbb{1}(\mathbf{x}_i \in Q_s) \mathbb{1}(y_i = y)}{\sum_{r \in \mathcal{P}} \sum_{s \in \mathcal{P}} \sum_{i=1}^n w_{rs} \mathbb{1}(\mathbf{x}_i \in Q_s) \mathbb{1}(y_i = y)}. \end{aligned}$$

As  $n \rightarrow \infty$ , the estimated weights  $w_{rs}$  should satisfy the condition:

$$(12) \quad w_{rs} \rightarrow \begin{cases} 0, & \text{if } Q_r \neq Q_s \\ 1, & \text{if } Q_r = Q_s. \end{cases}$$

For simplicity, we will describe the estimation procedure for  $w_{rs}$  in the next sections. Note that if we satisfy Condition 12, then we have  $\frac{\tilde{w}_{ry}}{\tilde{w}_y} \rightarrow \frac{n_{ry}}{n_y}$  as  $n \rightarrow \infty$ . Therefore, we modify Equation 5 as:

$$(13) \quad \tilde{f}_y(\mathbf{x}) = \frac{1}{\tilde{w}_y} \sum_{r \in \mathcal{P}} \tilde{w}_{ry} \mathcal{G}(\mathbf{x}; \hat{\mu}_r, \hat{\Sigma}_r) \mathbb{1}(r = \hat{r}_{\mathbf{x}}^*),$$



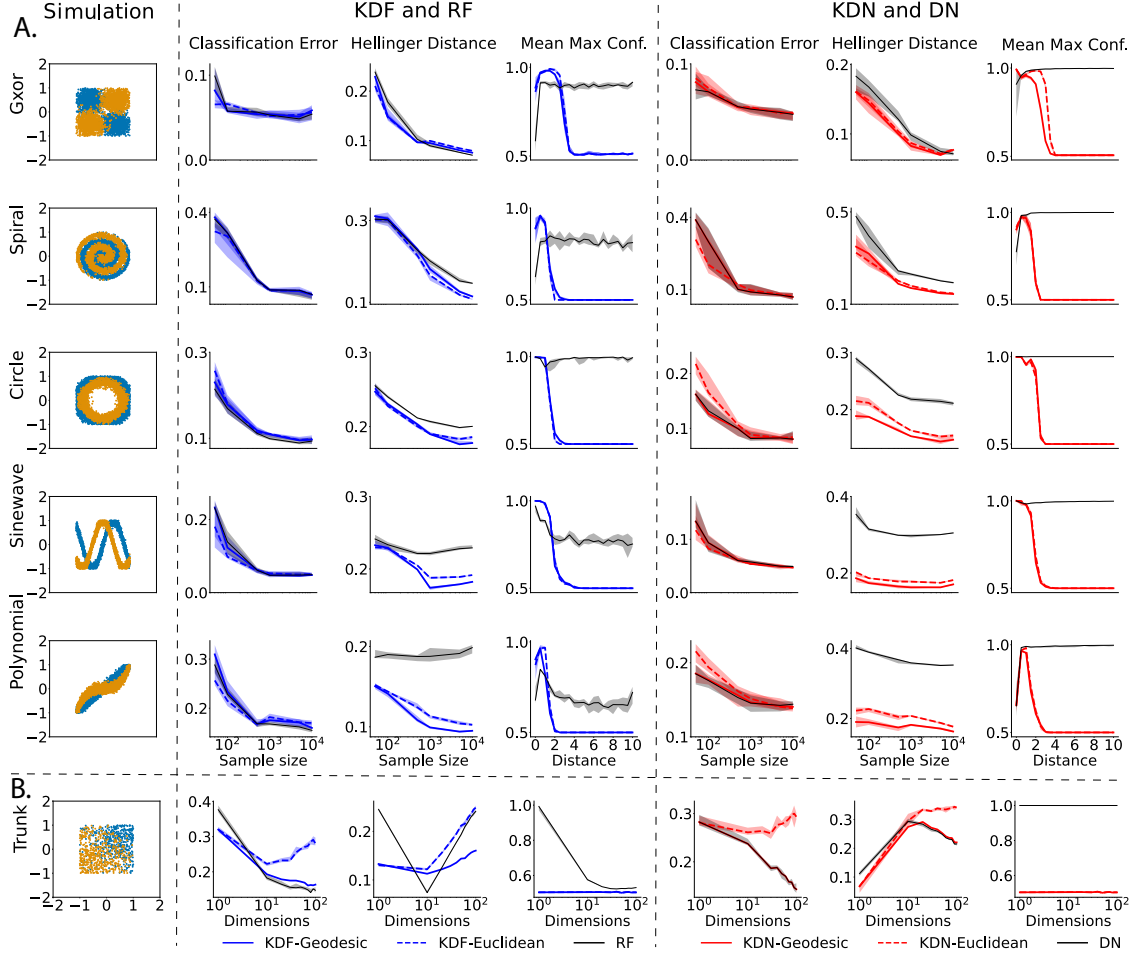


Figure 1: **Simulation datasets, Classification error, Hellinger distance from true posteriors, mean max confidence or posterior for A. five two-dimensional and B. a high dimensional (Trunk) simulation experiments.** The simulation experiments were repeated 45 times. The median performance is shown as a dark curve with shaded region as error bars showing the 25-th and the 75-th percentile. KDF and KDN improve both in- and out-of-distribution calibration of their respective parent algorithms while maintaining nearly similar classification accuracy on the simulation datasets. For Trunk simulation sample size was fixed at 5000 for gradually higher number of dimensions and OOD test samples were sampled uniformly from a hyper-sphere with radius fixed at 20. Trunk simulation dataset is visualized for the first two dimensions.

where  $\hat{r}_x^* = \operatorname{argmin}_r \|\hat{\mu}_r - \mathbf{x}\|$ . Now we use  $\tilde{f}_y(\mathbf{x})$  estimated using (13) in Equation (6), (7) and (8), respectively. Below, we describe how we estimate  $w_{rs}$  for KDF and KDN.

**4.3 Kernel Density Forest** Consider  $T$  number of decision trees in a random forest trained on  $n$  i.i.d training samples  $\{(\mathbf{x}_i, y_i)\}_{i=1}^n$ . Each tree  $t$  partitions the feature space into  $p_t$  polytopes resulting in a set of polytopes:  $\{\{Q_{t,r}\}_{r=1}^{p_t}\}_{t=1}^T$ . The intersection of these polytopes gives a new set of polytopes  $\{Q_r\}_{r=1}^R$  for the forest. For any point  $\mathbf{x}_r \in Q_r$ , we push every other sample point  $\mathbf{x}_s \in Q_s$  down the trees. We define the kernel  $\mathcal{K}(r, s)$  as:

$$(14) \quad \mathcal{K}(r, s) = \frac{t_{rs}}{T},$$

where  $t_{rs}$  is the total number of trees  $\mathbf{x}_r$  and  $\mathbf{x}_s$  end up in the same leaf node. Note that  $0 \leq \mathcal{K}(r, s) \leq 1$ . If the two samples end up in the same leaves in all the trees, i.e.,  $\mathcal{K}(r, s) = 1$ , they belong to the same polytope, i.e.  $r = s$ .

In short,  $\mathcal{K}(r, s)$  is the fraction of total trees where the two samples follow the same path from the

root to a leaf node. We exponentiate  $\mathcal{K}(r, s)$  so that Condition 12 is satisfied:

$$(15) \quad w_{rs} = \mathcal{K}(r, s)^{k \log n}.$$

We choose  $k$  using grid search on a hold-out dataset.

**4.4 Kernel Density Network** Consider a fully connected  $L$  layer ReLU-net trained on  $n$  iid training samples  $\{(\mathbf{x}_i, y_i)\}_{i=1}^n$ . We have the set of all nodes denoted by  $\mathcal{N}_l$  at a particular layer  $l$ . We can randomly pick a node  $n_l \in \mathcal{N}_l$  at each layer  $l$ , and construct a sequence of nodes starting at the input layer and ending at the output layer which we call an **activation path**:  $m = \{n_l \in \mathcal{N}_l\}_{l=1}^L$ . Note that there are  $N = \prod_{l=1}^L |\mathcal{N}_l|$  possible activation paths for a sample in the ReLU-net. We index each path by a unique identifier number  $z \in \mathbb{N}$  and construct a sequence of activation paths as:  $\mathcal{M} = \{m_z\}_{z=1, \dots, N}$ . Therefore,  $\mathcal{M}$  contains all possible activation pathways from the input to the output of the network.

While pushing a training sample  $\mathbf{x}_i$  through the network, we define the activation from a ReLU unit at any node as ‘1’ when it has non-negative input and ‘0’ otherwise. Therefore, the activation indicates on which side of the affine function at each node the sample falls. The activation for all nodes in an activation path  $m_z$  for a particular sample creates an **activation mode**  $a_z \in \{0, 1\}^L$ . If we evaluate the activation mode for all activation paths in  $\mathcal{M}$  while pushing a sample through the network, we get a sequence of activation modes:  $\mathcal{A}_r = \{a_z^r\}_{z=1}^N$ . Here  $r$  is the index of the polytope where the sample falls in.

*If the two sequences of activation modes for two different training samples are identical, they belong to the same polytope.* In other words, if  $\mathcal{A}_r = \mathcal{A}_s$ , then  $Q_r = Q_s$ . This statement holds because the above samples will lie on the same side of the affine function at each node in different layers of the network. Now, we define the kernel  $\mathcal{K}(r, s)$  as:

$$(16) \quad \mathcal{K}(r, s) = \frac{\sum_{z=1}^N \mathbb{1}(a_z^r = a_z^s)}{N}.$$

Note that  $0 \leq \mathcal{K}(r, s) \leq 1$ . In short,  $\mathcal{K}(r, s)$  is the fraction of total activation paths which are identically activated for two samples in two different polytopes  $r$  and  $s$ . We exponentiate the kernel using Equation 15.

Pseudocodes outlining the two algorithms are provided in Appendix C.

**4.5 Geodesic Distance** Consider  $\mathcal{P}_n = \{Q_1, Q_2, \dots, Q_R\}$  as a partition of  $\mathbb{R}^d$  given by a random forest or a ReLU-net after being trained on  $n$  training samples. We measure distance between two points  $\mathbf{x} \in Q_r, \mathbf{x}' \in Q_s$  using the kernel introduced in Equation 14 and Equation 16 [22] and call it ‘Geodesic’ distance:

$$(17) \quad d(r, s) = -\mathcal{K}(r, s) + \frac{1}{2}(\mathcal{K}(r, r) + \mathcal{K}(s, s)) = 1 - \mathcal{K}(r, s)$$

**Proposition 2.**  $(\mathcal{P}_n, d)$  is a metric space.

*Proof.* See Appendix A.1 for the proof. ■

As  $d$  cannot distinguish between points within the same polytope, it has a resolution similar to the size of the polytope. For discriminating between two points within the same polytope, we fit a Gaussian kernel within the polytope (described above). As  $h_n \rightarrow 0$ , the resolution for Geodesic distance improves. In Section 5, we will empirically show that using Geodesic distance scales better with higher dimension compared to that of Euclidean distance.

**Lemma 3.** For any two points,  $\mathbf{x}_1 \in Q_r$  and  $\mathbf{x}_2 \in Q_s$ , if  $d(r, s) = 0$ , that is,  $\mathcal{K}(r, s) = 1$ , we have  $r = s$ .

Given  $n$  independent and identically distributed training samples  $\{(\mathbf{x}_i, y_i)\}_{i=1}^n$ , we define the distance of an inference point  $\mathbf{x}$  from the training points as:  $d_{\mathbf{x}} = \min_{i=1, \dots, n} \|\mathbf{x} - \mathbf{x}_i\|$ .

**Proposition 4 (Asymptotic OOD Convergence).** *Given non-zero and bounded bandwidth of the Gaussians, then we have almost sure convergence for  $\hat{g}_y$  as:*

$$\lim_{d_{\mathbf{x}} \rightarrow \infty} \hat{g}_y(\mathbf{x}) = \hat{P}_Y(y).$$

**5 Empirical Results** We conduct several experiments on simulated, OpenML-CC18 [23]<sup>1</sup> and vision benchmark datasets to gain insights on the finite sample performance of KDF and KDN. The details of the simulation datasets and hyperparameters used for all the experiments are provided in Appendix B. For Trunk simulation dataset, we follow the simulation setup proposed by Trunk [24] which was designed to demonstrate ‘curse of dimensionality’. In the Trunk simulation, a binary class dataset is used where each class is sampled from a Gaussian distribution with higher dimensions having increasingly less discriminative information. We use both Euclidean and Geodesic distance in (4) on simulation datasets and use only Geodesic distance for benchmark datasets. For the simulation setups, we use classification error, hellinger distance [25, 26] from the true class conditional posteriors and mean max confidence or posterior [4] as performance statistics. While measuring in-distribution calibration for the datasets in OpenML-CC18 data suite, as we do not know the true distribution, we used maximum calibration error as defined by Guo et al. [18] with a fixed bin number of  $R = 15$  across all the datasets. Given  $n$  OOD samples, we define OOD calibration error (OCE) to measure OOD performance for the benchmark datasets as:

$$(18) \quad \text{OCE} = \frac{1}{n} \sum_{i=1}^n \left| \max_{y \in \mathcal{Y}} (\hat{P}_{Y|X}(y|\mathbf{x}_i)) - \max_{y \in \mathcal{Y}} (\hat{P}_Y(y)) \right|.$$

For the tabular and the vision datasets, we have used ID calibration approaches, such as ISOTONIC [15, 16] and SIGMOID [17] regression, as baselines. Additionally, for the vision benchmark dataset, we provide results with OOD calibration approaches such as: ACET [4], ODIN [6], OE (outlier exposure) [10]. We report traditionally used OOD detection statistics such as area under curve (AUROC) and false positive rate at 95% precision (FPR@95). For each approach, 90% of the training data was used to fit the model and the rest of the data was used to calibrate the model.

### 5.1 Empirical Study on Tabular Data

**Simulation Study** Figure 1 leftmost column shows 10000 training samples with 5000 samples per class sampled within the region  $[-1, 1] \times [-1, 1]$  from the six simulation setups described in Appendix B. Therefore, the empty annular region between  $[-1, 1] \times [-1, 1]$  and  $[-2, 2] \times [-2, 2]$  is the low density or OOD region in Figure 1. Figure 1 quantifies the performance of the algorithms which are visually represented in Appendix Figure 4. KDF and KDN maintain similar classification accuracy to those of their parent algorithms. We measure hellinger distance from the true distribution for increasing training sample size within  $[-1, 1] \times [-1, 1]$  region as a statistics for in-distribution calibration. Column 3 of left and Column 2 of right block in Figure 1 show KDF and KDN are better at estimating the high density region of training distribution compared to their parent methods. In all of the simulations, using geodesic distance measure results in better performance compared to those while using Euclidean distance. For measuring OOD performance, we keep the training sample size fixed at 1000 and normalize the training data by the maximum of their  $l_2$  norm so that the training data is confined within a unit circle. For inference, we sample 1000 inference points uniformly from a circle where the circles have increasing

<sup>1</sup><https://www.openml.org/s/99>

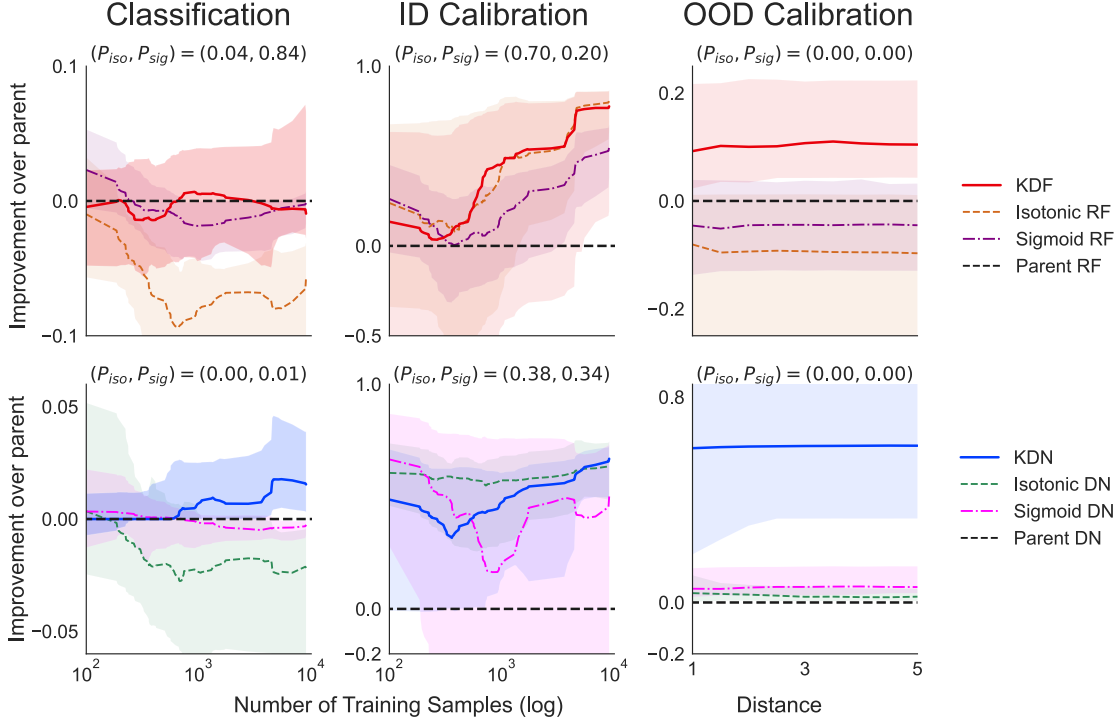


Figure 2: **Performance summary of KDF and KDN on OpenML-CC18 data suite.** The dark curve in the middle shows the median of performance on 45 datasets. The shaded region shows the error bar consisting of the 25-th and the 75-th percentile of the performance statistics. We conducted one-sided Wilcoxon rank-sum test using improvements in different datasets at the final sample size as test statistics. Each panel shows a p-value for each baseline approach which correspond to testing whether baseline model performs worse than our approach. **Left:** KDF and KDN maintains or improves performance of their parent algorithms for classification. **Middle:** KDF and KDN significantly improve the in-distribution calibration for random forest and ReLU-net. **Right:** Both of the proposed approaches yield highly calibrated confidence in the OOD region.

radius and plot mean max posterior for increasing distance from the origin. Therefore, for distance up to 1 we have in-distribution samples and distances farther than 1 can be considered as OOD region. As shown in Column 3 of Figure 1, mean max posteriors or confidence for KDF and KDN converge to the maximum of the class priors, i.e., 0.5 as we go farther away from the training data origin.

Row 6 of Figure 1 shows KDF-Geodesic and KDN-Geodesic scale better with higher dimensions compared to their Euclidean counterpart algorithms respectively.

**OpenML-CC18 Data Study** We use OpenML-CC18 data suite for tabular benchmark dataset study. We exclude any dataset which contains categorical features or NaN values<sup>2</sup> and conduct our experiments on 45 datasets with varying dimensions and sample sizes. For the OOD experiments, we follow a similar setup as that of the simulation data. We normalize the training data by their maximum  $l_2$  norm and sample 1000 testing samples uniformly from each hypersphere where the hyperspheres have increasing radius starting from 1 to 5. For each dataset, we measure improvement with respect to the parent algorithm as:

$$(19) \quad \frac{\mathcal{E}_p - \mathcal{E}_M}{\mathcal{E}_p},$$

where  $\mathcal{E}_p$  =classification error, MCE or OCE for the parent algorithm and  $\mathcal{E}_M$  represents the performance of the approach in consideration. Note that positive improvement implies the corresponding

<sup>2</sup>We also excluded the dataset with dataset id 23517 as we could not achieve better than chance accuracy using RF and DN on that dataset.

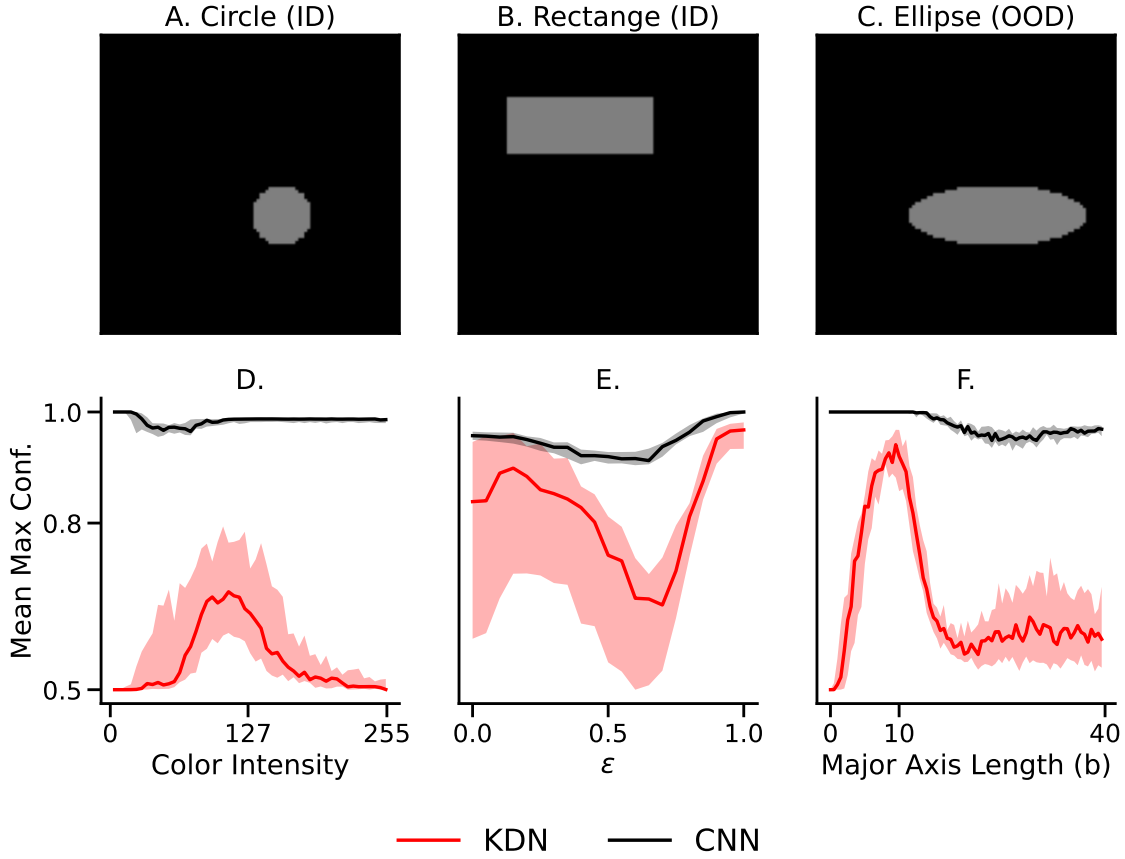


Figure 3: KDN filters out inference points with different kinds of semantic shifts from the training data. Simulated images used as training points: (A) circle with radius 10, (B) rectangle with sides (20, 50) and out-of-distribution test points: (C) ellipse with minor and major axis (10, 30). For the above images, RGB intensities are fixed at [127, 127, 127]. Mean max confidence of KDN are plotted for semantic shift of the inference points created by (D) changing the color intensity, (E) taking convex combination of circle and rectangle, i.e.,  $\epsilon \times \text{circle} + (1 - \epsilon) \times \text{rectangle}$ , (F) changing one of the axes of the ellipse. Note that for  $b = 10$ , the ellipse becomes a circle (ID).

approach performs better than the parent approach. We report the median of improvement on different datasets along with the error bar in Figure 2. The extended results for each dataset is shown separately in the appendix. Figure 2 left column shows on average KDF and KDN has nearly similar or better classification accuracy to their respective parent algorithm whereas ISOTONIC and SIGMOID regression have lower classification accuracy most of the cases. However, according to Figure 2 middle column, KDF and KDN have similar in-distribution calibration performance to the other baseline approaches. Most interestingly, Figure 2 right column shows that KDN and KDF improves OOD calibration of their respective parent algorithms by a huge margin while the baseline approaches completely fails to address the OOD calibration problem.

**5.2 Empirical Study on Vision Data** In vision data, each image pixel contains local information about the neighboring pixels. To extract the local information, we use the convolutional layers at the front-end of a convolutional neural network (CNN). More precisely, we have a convolutional front-end encoder,  $h_e : \mathbb{R}^D \mapsto \mathbb{R}^m$  and typically,  $m \ll D$ . After the encoder there is a few fully connected dense layers for discriminating among the  $K$  class labels,  $h_f : \mathbb{R}^m \mapsto \mathbb{R}^K$ . We fit a KDN on the  $m$ -dimensional embedding outputs from the encoder and measure our proposed kernel in Equation (16) on the dense layers.

**Simulation Study** For the simulation study, we use a simple CNN with one convolutional layer (3 channels with  $3 \times 3$  kernel) followed by two fully connected layers with 10 and 2 nodes in each. We train the CNN on 2000 circle (radius 10) and 2000 rectangle (sides 20, 50) images with their RGB values being fixed at  $[127, 127, 127]$  and their centers randomly sampled within a square with sides 100. The other pixels in the background where there is no object (circle, rectangle or ellipse) were set to 0.

We perform three experiments while inducing semantic shifts in the inference points as shown in Figure 3. In the first experiment, we randomly sampled data similar to the training points. However, we added the same shift to all the RGB values of an inference point (shown as color intensity in Figure 3 D). Therefore, the inference point is ID for color intensity at 127 and otherwise OOD. In the second experiment, we kept the RGB values fixed at  $[127, 127, 127]$  while taking convex combination of a circle and a rectangle. Let images of circles and rectangles be denoted by  $X_c$  and  $X_r$ . We derive an interference point as  $X_{inf}$ :

$$(20) \quad X_{inf} = \epsilon X_c + (1 - \epsilon) X_r$$

Therefore,  $X_{inf}$  is maximally distant from the training points for  $\epsilon = 0.5$  and closest to the ID points at  $\epsilon = 0, 1$ . In the third experiment, we sampled ellipse images with the same RGB values as the training points. However, this time we gradually change one of the ellipse axes from 0.01 to 40 while keeping the other axis fixed at 10. As a result, the inference point becomes ID for the axis length of 10. As shown in Figure 3 (D, E, F), in all the experiments KDN becomes less confident for the OOD points while the parent CNN remains overconfident throughout the semantic shifts of the inference points. The above property shown by KDN is highly desirable in a learning algorithm as the model is resonant or tuned to the training inputs and suppresses anything that deviates from the training concepts.

Table 1: KDN achieves better calibration compared to different algorithms on different datasets when trained on CIFAR-10. ‘↑’ and ‘↓’ indicate whether higher and lower values are better, respectively. Bolded indicates most performant, or within the margin of error of the most performant.

	Dataset	Statistics	Parent	KDN	ISOTONIC	SIGMOID	ACET	ODIN	OE
ID	CIFAR-10	Accuracy(%) ↑ MCE ↓	77.78 ± 0.00 0.09 ± 0.00	76.84 ± 0.01 <b>0.04</b> ± 0.00	<b>78.25</b> ± 0.00 <b>0.03</b> ± 0.01	76.93 ± 0.00 0.10 ± 0.01	75.08 ± 0.03 0.13 ± 0.00	78.00 ± 0.00 0.09 ± 0.00	73.95 ± 0.00 0.55 ± 0.00
OOD	CIFAR-100	AUROC ↑	0.82 ± 0.00	<b>0.83</b> ± 0.00	<b>0.83</b> ± 0.00	0.80 ± 0.00	0.81 ± 0.00	0.81 ± 0.00	0.81 ± 0.00
		FPR@95 ↓	<b>0.50</b> ± 0.33	<b>0.50</b> ± 0.26	<b>0.54</b> ± 0.26	<b>0.51</b> ± 0.32	<b>0.56</b> ± 0.27	<b>0.49</b> ± 0.33	<b>0.45</b> ± 0.35
		OCE ↓	0.30 ± 0.00	0.20 ± 0.01	0.37 ± 0.01	0.29 ± 0.01	0.55 ± 0.00	0.31 ± 0.00	<b>0.01</b> ± 0.00
	SVHN	AUROC ↑	0.27 ± 0.00	<b>1.00</b> ± 0.00	0.22 ± 0.03	0.20 ± 0.07	0.36 ± 0.04	0.27 ± 0.01	0.70 ± 0.01
		FPR@95 ↓	0.58 ± 0.42	<b>0.14</b> ± 0.11	0.63 ± 0.35	0.59 ± 0.41	0.64 ± 0.36	0.58 ± 0.43	0.54 ± 0.44
		OCE ↓	0.87 ± 0.00	<b>0.01</b> ± 0.00	0.85 ± 0.00	0.69 ± 0.01	0.90 ± 0.00	0.87 ± 0.00	0.04 ± 0.01
	Noise	AUROC ↑	0.20 ± 0.00	<b>1.00</b> ± 0.00	0.36 ± 0.07	0.24 ± 0.09	<b>1.00</b> ± 0.00	0.97 ± 0.00	0.97 ± 0.02
		FPR@95 ↓	0.58 ± 0.42	<b>0.12</b> ± 0.12	0.64 ± 0.36	0.59 ± 0.41	0.38 ± 0.38	<b>0.08</b> ± 0.08	<b>0.15</b> ± 0.29
		OCE ↓	0.90 ± 0.00	<b>0.00</b> ± 0.00	0.87 ± 0.00	0.71 ± 0.00	0.01 ± 0.01	0.06 ± 0.00	<b>0.00</b> ± 0.00

**Vision Benchmark Datasets Study** For vision benchmark experiments, we use a RESNET-50 encoder pretrained using contrastive loss [27] as described in <http://keras.io/examples/vision/supervised-contrastive-learning/>. The encoder projects the input images down to a 256 dimensional latent space and we add two dense layers with 200 and 10 nodes on top of the encoder. We use the same pretrained encoder for all the baseline algorithms.

As shown in Table 1, KDN achieves good calibration for both ID and OOD datasets whereas the ID calibration approaches are poorly calibrated in the OOD regions and the OOD approaches have poor ID calibration.

**6 Discussion** In this paper, we convert deep discriminative algorithms to kernel density graph by replacing the affine function over the polytopes in the discriminative networks with a Gaussian kernel. This replacement of affine function results in better in- and out-of-distribution calibration for our proposed approaches both on tabular and vision benchmark datasets. Our code, including the package and the experiments in this manuscript, will be made publicly available upon acceptance of the paper.



**Acknowledgements** The authors thank the support of the NSF-Simons Research Collaborations on the Mathematical and Scientific Foundations of Deep Learning (NSF grant 2031985) and THEORINET. This work is graciously supported by the Defense Advanced Research Projects Agency (DARPA) Life-long Learning Machines program through contracts FA8650-18-2-7834 and HR0011-18-2-0025. Research was partially supported by funding from Microsoft Research and the Kavli Neuroscience Discovery Institute.

## References

- [1] Chuan Guo, Geoff Pleiss, Yu Sun, and Kilian Q. Weinberger. On calibration of modern neural networks. In Doina Precup and Yee Whye Teh, editors, Proceedings of the 34th International Conference on Machine Learning, volume 70 of Proceedings of Machine Learning Research, pages 1321–1330. PMLR, 06–11 Aug 2017.
- [2] Agustinus Kristiadi, Matthias Hein, and Philipp Hennig. Being bayesian, even just a bit, fixes overconfidence in ReLU networks. In Hal Daumé III and Aarti Singh, editors, Proceedings of the 37th International Conference on Machine Learning, volume 119 of Proceedings of Machine Learning Research, pages 5436–5446. PMLR, 13–18 Jul 2020.
- [3] Haoyin Xu, Kaleab A. Kinfe, Will LeVine, Sambit Panda, Jayanta Dey, Michael Ainsworth, Yu-Chung Peng, Madi Kusmanov, Florian Engert, Christopher M. White, Joshua T. Vogelstein, and Carey E. Priebe. When are Deep Networks really better than Decision Forests at small sample sizes, and how? arXiv preprint arXiv:2108.13637, 2021.
- [4] Matthias Hein, Maksym Andriushchenko, and Julian Bitterwolf. Why relu networks yield high-confidence predictions far away from the training data and how to mitigate the problem. In Proceedings of the IEEE/CVF Conference on Computer Vision and Pattern Recognition, pages 41–50, 2019.
- [5] Alexander Meinke, Julian Bitterwolf, and Matthias Hein. Provably robust detection of out-of-distribution data (almost) for free. arXiv preprint arXiv:2106.04260, 2021.
- [6] Shiyu Liang, Yixuan Li, and Rayadurgam Srikant. Enhancing the reliability of out-of-distribution image detection in neural networks. arXiv preprint arXiv:1706.02690, 2017.
- [7] Jay Nandy, Wynne Hsu, and Mong Li Lee. Towards maximizing the representation gap between in-domain & out-of-distribution examples. Advances in Neural Information Processing Systems, 33:9239–9250, 2020.
- [8] Weitao Wan, Yuanyi Zhong, Tianpeng Li, and Jiansheng Chen. Rethinking feature distribution for loss functions in image classification. In Proceedings of the IEEE conference on computer vision and pattern recognition, pages 9117–9126, 2018.
- [9] Terrance DeVries and Graham W Taylor. Learning confidence for out-of-distribution detection in neural networks. arXiv preprint arXiv:1802.04865, 2018.
- [10] Dan Hendrycks, Mantas Mazeika, and Thomas Dietterich. Deep anomaly detection with outlier exposure. arXiv preprint arXiv:1812.04606, 2018.
- [11] Jie Ren, Peter J Liu, Emily Fertig, Jasper Snoek, Ryan Poplin, Mark Depristo, Joshua Dillon, and Balaji Lakshminarayanan. Likelihood ratios for out-of-distribution detection. Advances in neural information processing systems, 32, 2019.
- [12] Diederik P Kingma, Max Welling, et al. An introduction to variational autoencoders. Foundations and Trends® in Machine Learning, 12(4):307–392, 2019.
- [13] Ian Goodfellow, Jean Pouget-Abadie, Mehdi Mirza, Bing Xu, David Warde-Farley, Sherjil Ozair, Aaron Courville, and Yoshua Bengio. Generative adversarial networks. Communications of the ACM, 63(11):139–144, 2020.
- [14] Eric Nalisnick, Akihiro Matsukawa, Yee Whye Teh, Dilan Gorur, and Balaji Lakshminarayanan. Do deep generative models know what they don’t know? arXiv preprint arXiv:1810.09136, 2018.

- [15] Bianca Zadrozny and Charles Elkan. Obtaining calibrated probability estimates from decision trees and naive bayesian classifiers. In lcm1, volume 1, pages 609–616, 2001.
- [16] R Caruana. Predicting good probabilities with supervised learning. In Proceedings of NIPS 2004 Workshop on Calibration and Probabilistic Prediction in Supervised Learning, 2004.
- [17] John Platt et al. Probabilistic outputs for support vector machines and comparisons to regularized likelihood methods. Advances in large margin classifiers, 10(3):61–74, 1999.
- [18] Chuan Guo, Geoff Pleiss, Yu Sun, and Kilian Q Weinberger. On calibration of modern neural networks. In International conference on machine learning, pages 1321–1330. PMLR, 2017.
- [19] Richard Guo, Ronak Mehta, Jesus Arroyo, Hayden Helm, Cencheng Shen, and Joshua T Vogelstein. Estimating information-theoretic quantities with uncertainty forests. arXiv, pages arXiv–1907, 2019.
- [20] Meelis Kull, Miquel Perello Nieto, Markus Kängsepp, Telmo Silva Filho, Hao Song, and Peter Flach. Beyond temperature scaling: Obtaining well-calibrated multi-class probabilities with dirichlet calibration. Advances in neural information processing systems, 32, 2019.
- [21] Haoyin Xu, Kaleab A Kinfu, Will LeVine, Sambit Panda, Jayanta Dey, Michael Ainsworth, Yu-Chung Peng, Madi Kusmanov, Florian Engert, Christopher M White, et al. When are deep networks really better than decision forests at small sample sizes, and how? arXiv preprint arXiv:2108.13637, 2021.
- [22] Bernhard Schölkopf. The kernel trick for distances. Advances in neural information processing systems, 13, 2000.
- [23] Bernd Bischl, Giuseppe Casalicchio, Matthias Feurer, Pieter Gijsbers, Frank Hutter, Michel Lang, Rafael G Mantovani, Jan N van Rijn, and Joaquin Vanschoren. Openml benchmarking suites. arXiv preprint arXiv:1708.03731, 2017.
- [24] Gerard V Trunk. A problem of dimensionality: A simple example. IEEE Transactions on pattern analysis and machine intelligence, (3):306–307, 1979.
- [25] Thomas Kailath. The divergence and bhattacharyya distance measures in signal selection. IEEE transactions on communication technology, 15(1):52–60, 1967.
- [26] C Radhakrishna Rao. A review of canonical coordinates and an alternative to correspondence analysis using hellinger distance. Qüestiió: quaderns d’estadística i investigació operativa, 1995.
- [27] Prannay Khosla, Piotr Teterwak, Chen Wang, Aaron Sarna, Yonglong Tian, Phillip Isola, Aaron Maschinot, Ce Liu, and Dilip Krishnan. Supervised contrastive learning. Advances in neural information processing systems, 33:18661–18673, 2020.

## Appendix A. Proofs.

**A.1 Proof of Proposition 2** For proving that  $d$  is a valid distance metric for  $\mathcal{P}_n$ , we need to prove the following four statements:

1.  $d(r, s) = 0$  when  $r = s$ .

**Proof:** By definition,  $\mathcal{K}(r, s) = 1$  and  $d(r, s) = 0$  when  $r = s$ .

2.  $d(r, s) > 0$  when  $r \neq s$ .

**Proof:** By definition,  $0 \leq \mathcal{K}(r, s) < 1$  and  $d(r, s) > 0$  for  $r \neq s$ .

3.  $d$  is symmetric, i.e.,  $d(r, s) = d(s, r)$ .

**Proof:** By definition,  $\mathcal{K}(r, s) = \mathcal{K}(s, r)$  which implies  $d(r, s) = d(s, r)$ .

4.  $d$  follows the triangle inequality, i.e., for any three polytopes  $Q_r, Q_s, Q_t \in \mathcal{P}_n$ :  $d(r, t) \leq d(r, s) + d(s, t)$ .

**Proof:** Let  $\mathcal{A}_r$  denote the set of activation modes in a ReLU-net and the set of leaf nodes in a random forest for a particular polytope  $r$ .  $N$  is the total number of possible activation paths in a ReLU-net or total trees in a random forest. We can write:

$$\begin{aligned}
 (21) \quad N &\geq n((\mathcal{A}_r \cap \mathcal{A}_s) \cup (\mathcal{A}_s \cap \mathcal{A}_t)) \\
 &= n(\mathcal{A}_r \cap \mathcal{A}_s) + n(\mathcal{A}_s \cap \mathcal{A}_t) - n(\mathcal{A}_r \cap \mathcal{A}_s \cap \mathcal{A}_t) \\
 &\geq n(\mathcal{A}_r \cap \mathcal{A}_s) + n(\mathcal{A}_s \cap \mathcal{A}_t) - n(\mathcal{A}_r \cap \mathcal{A}_t)
 \end{aligned}$$

Rearranging the above equation, we get:

$$\begin{aligned}
 N - n(\mathcal{A}_r \cap \mathcal{A}_t) &\leq N - n(\mathcal{A}_r \cap \mathcal{A}_s) + N - n(\mathcal{A}_s \cap \mathcal{A}_t) \\
 \implies 1 - \frac{n(\mathcal{A}_r \cap \mathcal{A}_t)}{N} &\leq 1 - \frac{n(\mathcal{A}_r \cap \mathcal{A}_s)}{N} + 1 \\
 &\quad - \frac{n(\mathcal{A}_s \cap \mathcal{A}_t)}{N} \\
 (22) \quad \implies d(r, t) &\leq d(r, s) + d(s, t)
 \end{aligned}$$

**A.2 Proof of Proposition 4** We first expand  $\hat{g}_y(\mathbf{x})$ :

$$\begin{aligned}
 \hat{g}_y(\mathbf{x}) &= \frac{\hat{f}_y(\mathbf{x})\hat{P}_Y(y)}{\sum_{k=1}^K \hat{f}_k(x)\hat{P}_Y(k)} \\
 &= \frac{\hat{f}_y(\mathbf{x})\hat{P}_Y(y) + \frac{b}{\log(n)}\hat{P}_Y(y)}{\sum_{k=1}^K (\hat{f}_k(\mathbf{x})\hat{P}_Y(k) + \frac{b}{\log(n)}\hat{P}_Y(k))}
 \end{aligned}$$

As the inference point  $\mathbf{x}$  becomes more distant from training samples (and more distant from all of the Gaussian centers), we have that  $\mathcal{G}(\mathbf{x}, \hat{\mu}_r, \hat{\Sigma}_r)$  becomes smaller. Thus,  $\forall y, \tilde{f}_y(\mathbf{x})$  shrinks. More formally,  $\forall y$ ,

$$\lim_{d_{\mathbf{x}} \rightarrow \infty} \tilde{f}_y(\mathbf{x}) = 0$$

We can use this result to then examine the limiting behavior of our posteriors as the inference point  $\mathbf{x}$  becomes more distant from the training data:

$$\begin{aligned}
\lim_{d_{\mathbf{x}} \rightarrow \infty} \hat{g}_y(\mathbf{x}) &= \lim_{d_{\mathbf{x}} \rightarrow \infty} \frac{\tilde{f}_y(\mathbf{x}) \hat{P}_Y(y) + \frac{b}{\log(n)} \hat{P}_Y(y)}{\sum_{k=1}^K (\tilde{f}_k(\mathbf{x}) \hat{P}_Y(k) + \frac{b}{\log(n)} \hat{P}_Y(k))} \\
&= \frac{(\lim_{d_{\mathbf{x}} \rightarrow \infty} \tilde{f}_y(\mathbf{x})) \hat{P}_Y(y) + \frac{b}{\log(n)} \hat{P}_Y(y)}{\sum_{k=1}^K (\lim_{d_{\mathbf{x}} \rightarrow \infty} \tilde{f}_k(\mathbf{x})) \hat{P}_Y(k) + \frac{b}{\log(n)} \hat{P}_Y(k)} \\
&= \frac{\hat{P}_Y(y)}{\sum_{k=1}^K \hat{P}_Y(k)} \\
&= \hat{P}_Y(y)
\end{aligned}$$

## Appendix B. Simulations.

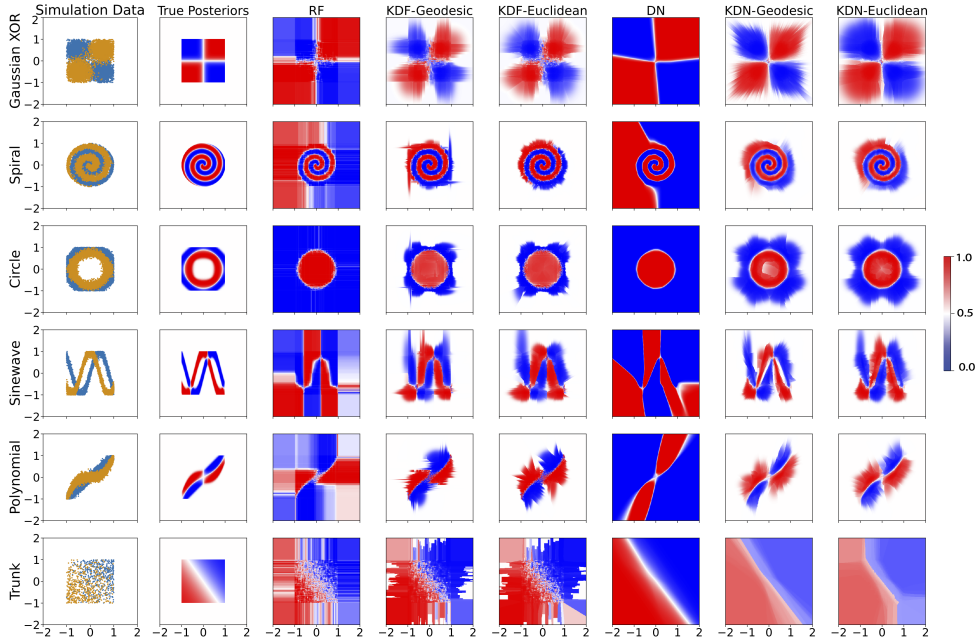


Figure 4: **Visualization of true and estimated posteriors for class 0 from five binary class simulation experiments.** *Column 1:* 10,000 training points with 5,000 samples per class sampled from 6 different simulation setups for binary class classification. Trunk simulation is shown for two dimensional case. The class labels are indicated by yellow and blue colors. *Column 2-8:* True and estimated class conditional posteriors from different approaches. The posteriors estimated from KDN and KDF are better calibrated for both in- and out-of-distribution regions compared to those of their parent algorithms.

We construct six types of binary class simulations:

- *Gaussian XOR* is a two-class classification problem with equal class priors. Conditioned on being in class 0, a sample is drawn from a mixture of two Gaussians with means  $\pm[0.5, -0.5]^\top$  and standard deviations of 0.25. Conditioned on being in class 1, a sample is drawn from a mixture of two Gaussians with means  $\pm[0.5, -0.5]^\top$  and standard deviations of 0.25.
- *Spiral* is a two-class classification problem with the following data distributions: let  $K$  be the number of classes and  $S \sim \text{multinomial}(\frac{1}{K} \mathbf{1}_K, n)$ . Conditioned on  $S$ , each feature vector is parameterized by two variables, the radius  $r$  and an angle  $\theta$ . For each sample,  $r$  is sampled uniformly in  $[0, 1]$ . Conditioned on a particular class, the angles are evenly spaced between  $\frac{4\pi(k-1)t_K}{K}$  and  $\frac{4\pi(k)t_K}{K}$ , where  $t_K$  controls the number of turns in the spiral. To inject noise along

the spirals, we add Gaussian noise to the evenly spaced angles  $\theta' : \theta = \theta' + \mathcal{N}(0, 0.09)$ . The observed feature vector is then  $(r \cos(\theta), r \sin(\theta))$ .

- *Circle* is a two-class classification problem with equal class priors. Conditioned on being in class 0, a sample is drawn from a circle centered at  $(0, 0)$  with a radius of  $r = 0.75$ . Conditioned on being in class 1, a sample is drawn from a circle centered at  $(0, 0)$  with a radius of  $r = 1$ , which is cut off by the region bounds. To inject noise along the circles, we add Gaussian noise to the circle radii  $r' : r = r' + \mathcal{N}(0, 0.01)$ .
- *Sinewave* is a two-class classification problem based on sine waves. Conditioned on being in class 0, a sample is drawn from the distribution  $y = \cos(\pi x)$ . Conditioned on being in class 1, a sample is drawn from the distribution  $y = \sin(\pi x)$ . We inject Gaussian noise to the sine wave heights  $y' : y = y' + \mathcal{N}(0, 0.01)$ .
- *Polynomial* is a two-class classification problem with the following data distributions:  $y = x^a$ . Conditioned on being in class 0, a sample is drawn from the distribution  $y = x^1$ . Conditioned on being in class 1, a sample is drawn from the distribution  $y = x^3$ . Gaussian noise is added to variables  $y' : y = y' + \mathcal{N}(0, 0.01)$ .
- *Trunk* is a two-class classification problem with gradually increasing dimension and equal class priors. The class conditional probabilities are Gaussian:

$$P(X|Y = 0) = \mathcal{G}(\mu_1, I),$$

$$P(X|Y = 1) = \mathcal{G}(\mu_2, I),$$

where  $\mu_1 = \mu, \mu_2 = -\mu$ ,  $\mu$  is a  $d$  dimensional vector whose  $i$ -th component is  $(\frac{1}{i})^{1/2}$  and  $I$  is  $d$  dimensional identity matrix.

Table 2: Hyperparameters for RF and KDF.

Hyperparameters	Value
n_estimators	500
max_depth	$\infty$
min_samples_leaf	1
$\lambda$	$1 \times 10^{-6}$

Table 3: Hyperparameters for ReLU-net and KDN.

Hyperparameters	Value
number of hidden layers	4
nodes per hidden layer	1000
optimizer	Adam
learning rate	$3 \times 10^{-4}$
$\lambda$	$1 \times 10^{-6}$

**Appendix C. Pseudocodes.** We provide the pseudocode for our proposed algorithms in Algorithm 1, 2 and 3.

**Appendix D. Time Complexity.** Time complexity for KDF and KDN  $O(mn^2)$ , where  $m$  = total number of leaves in the forest or total nodes in the dense layers of the network and  $n$  = total training samples.

#### Appendix E. Hardware and Software Configurations.

- Operating System: Linux (ubuntu 20.04), macOS (Ventura 13.2.1)
- VM Size: Azure Standard D96as v4 (96 vcpus, 384 GiB memory)

---

**Algorithm 1** Fit a KGX model.

---

**Input:**

- (1)  $\theta$  ▷ Parent learner (random forest or deep network model)  
(2)  $\mathcal{D}_n = (\mathbf{X}, \mathbf{y}) \in \mathbb{R}^{n \times d} \times \{1, \dots, K\}^n$  ▷ Training data

**Output:**  $\mathcal{G}$  ▷ a KGX model

```
1: function KGX.FIT( $\theta, \mathbf{X}, \mathbf{y}$ )  
2:   for  $i = 1, \dots, n$  do ▷ Iterate over the dataset to calculate the weights  
3:     for  $j = 1, \dots, n$  do  
4:        $w_{ij} \leftarrow \text{COMPUTEWEIGHTS}(\mathbf{x}_i, \mathbf{x}_j, \theta)$   
5:     end for  
6:   end for  
7:  
8:  
9:    $\{Q_r\}_{r=1}^{\tilde{p}} \leftarrow \text{GETPOLYTOPES}(\mathbf{w})$  ▷ Identify the polytopes by clustering the samples with similar weight  
10:  
11:    $\mathcal{G}.\{\tilde{w}_k\}_{k=1}^K \leftarrow 0$  ▷ Initialize the counts for each class  
12:   for  $r = 1, \dots, \tilde{p}$  do ▷ Iterate over each polytope  
13:     for  $k = 1, \dots, K$  do  
14:        $\mathcal{G}.\tilde{w}_{rk} \leftarrow \text{COUNTWEIGHTS}(\{\mathbf{w}_{rs}\}_{s=1}^{\tilde{p}}, k)$  ▷  $w_{rk}$  is the number of weighted input samples in  $Q_r$  with label  $k$   
15:        $\mathcal{G}.\tilde{w}_k \leftarrow \mathcal{G}.\tilde{w}_k + \mathcal{G}.\tilde{w}_{rk}$  ▷ Update the total count for each class  
16:     end for  
17:      $\mathcal{G}.\hat{\mu}_r, \mathcal{G}.\hat{\Sigma}_r \leftarrow \text{ESTIMATEPARAMETERS}(\mathbf{X}, \{\mathbf{w}_{rs}\}_{s=1}^{\tilde{p}})$  ▷ Fit Gaussians using weighted MLE  
18:   end for  
19:   return  $\mathcal{G}$   
20: end function
```

---

---

**Algorithm 2** Computing weights in KDF

---

**Input:**

- (1)  $\mathbf{x}_i, \mathbf{x}_j \in \mathbb{R}^{1 \times d}$  ▷ two input samples to be weighted  
(2)  $\theta$  ▷ parent random forest with  $T$  trees

**Output:**  $w_{ij} \in [0, 1]$  ▷ compute similarity between  $i$  and  $j$ -th samples.

```
1: function COMPUTEWEIGHTS( $\mathbf{x}_i, \mathbf{x}_j, \theta$ )  
2:    $\mathcal{I}_i \leftarrow \text{PUSHDOWNTREES}(\mathbf{x}_i, \theta)$  ▷ push  $\mathbf{x}_i$  down  $T$  trees and get the leaf numbers it end up in.  
3:    $\mathcal{I}_j \leftarrow \text{PUSHDOWNTREES}(\mathbf{x}_j, \theta)$  ▷ push  $\mathbf{x}_j$  down  $T$  trees and get the leaf numbers it end up in.  
4:    $l \leftarrow \text{COUNTMATCHES}(\mathcal{I}_i, \mathcal{I}_j)$  ▷ count the number of times the samples end up in the same leaf  
5:    $w_{ij} \leftarrow \frac{l}{T}$   
6:   return  $w_{ij}$   
7: end function
```

---

- GPU: Apple M1 Max
- Software: Python 3.8, scikit-learn  $\geq 0.22.0$ , tensorflow-macos  $\leq 2.9$ , tensorflow-metal  $\leq 0.5.0$ .



---

**Algorithm 3** Computing weights in KDN

---

**Input:**(1)  $\mathbf{x}_i, \mathbf{x}_j \in \mathbb{R}^{1 \times d}$ 

▷ two input samples to be weighted

(2)  $\theta$ 

▷ parent deep-net model

**Output:**  $w_{ij} \in [0, 1]$ ▷ compute similarity between  $i$  and  $j$ -th samples.1: **function** COMPUTEWEIGHTS( $\mathbf{x}_i, \mathbf{x}_j, \theta$ )2:  $\mathcal{A}_i \leftarrow \text{PUSHDOWNNETWORK}(\mathbf{x}_i, \theta)$ ▷ get activation modes  $\mathcal{A}_i$ 3:  $\mathcal{A}_j \leftarrow \text{PUSHDOWNNETWORK}(\mathbf{x}_j, \theta)$ ▷ get activation modes  $\mathcal{A}_j$ 4:  $l \leftarrow \text{COUNTMATCHES}(\mathcal{A}_i, \mathcal{A}_j)$ 

▷ count the number of times the two samples activate the

activation paths in a similar way

5:  $w_{ij} \leftarrow \frac{l}{N}$ ▷  $N$  is the total number of activation paths6: **return**  $w_{ij}$ 7: **end function**

---

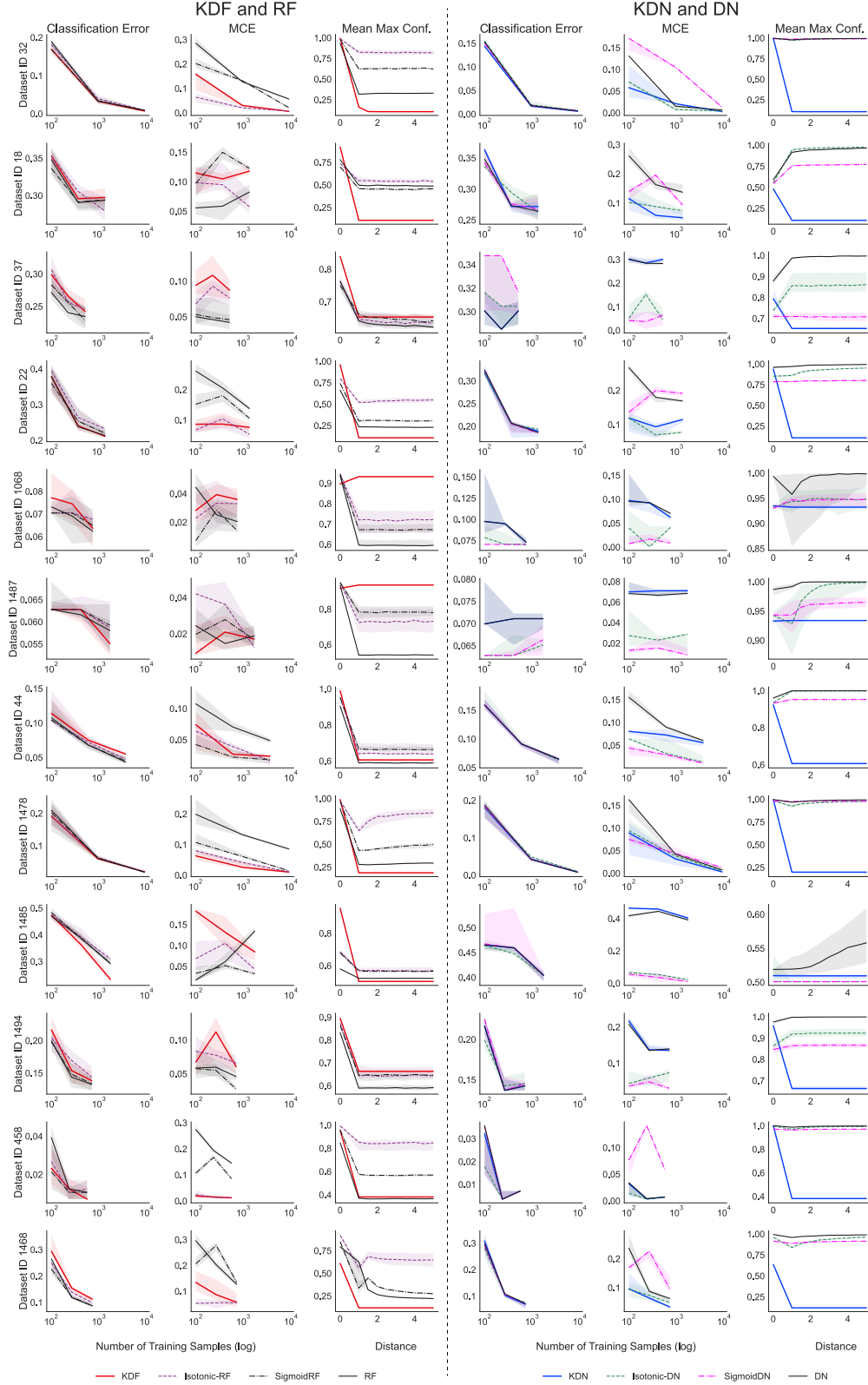


Figure 5: **Extended results on OpenML-CC18 datasets.** *Left:* Performance (classification error, MCE and mean max confidence) of KDF on different Openml-CC18 datasets. *Right:* Performance (classification error, MCE and mean max confidence) of KDN on different Openml-CC18 datasets.

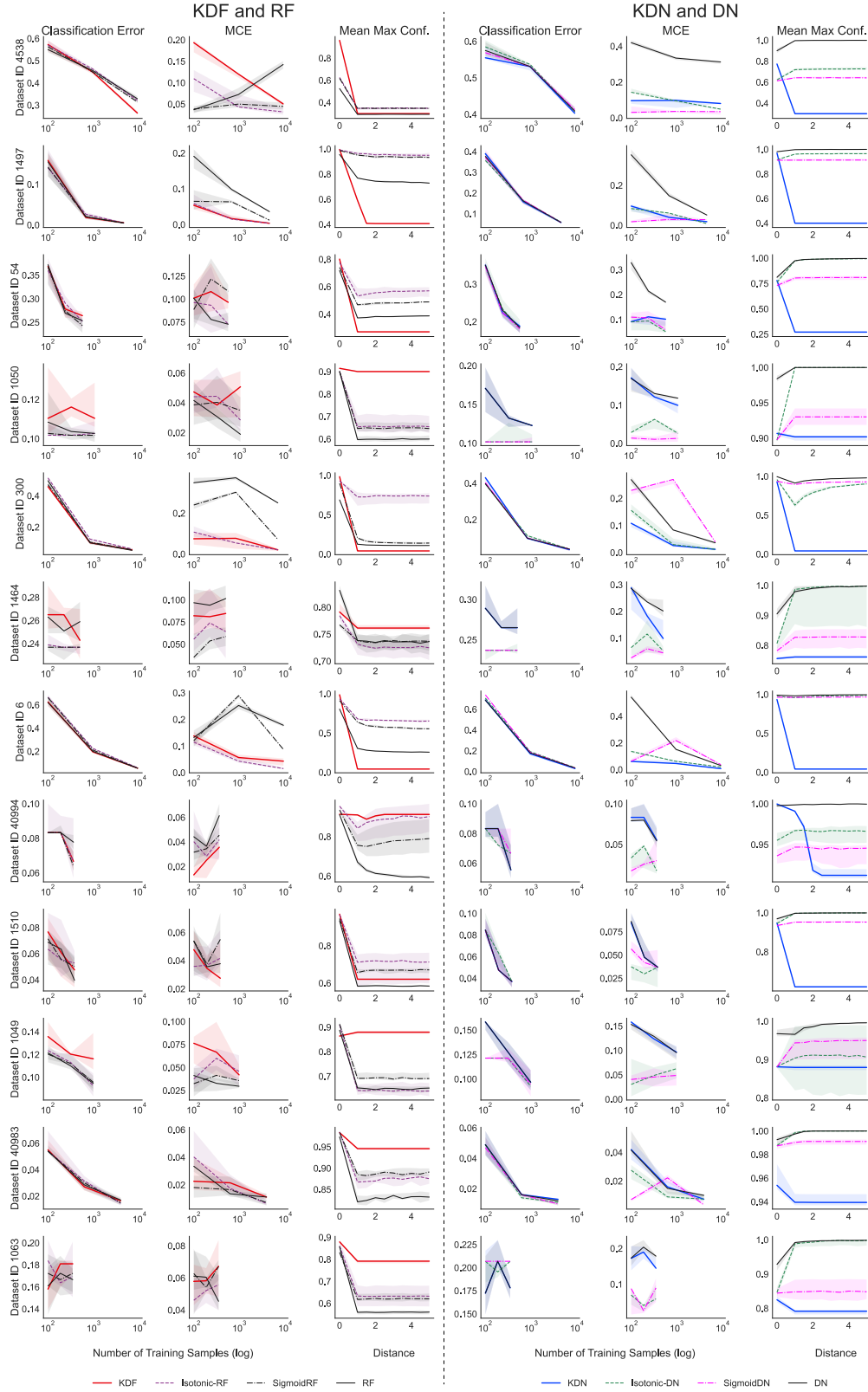


Figure 6: **Extended results on OpenML-CC18 datasets (continued).** *Left:* Performance (classification error, MCE and mean max confidence) of KDF on different Openml-CC18 datasets. *Right:* Performance (classification error, MCE and mean max confidence) of KDN on different Openml-CC18 datasets.

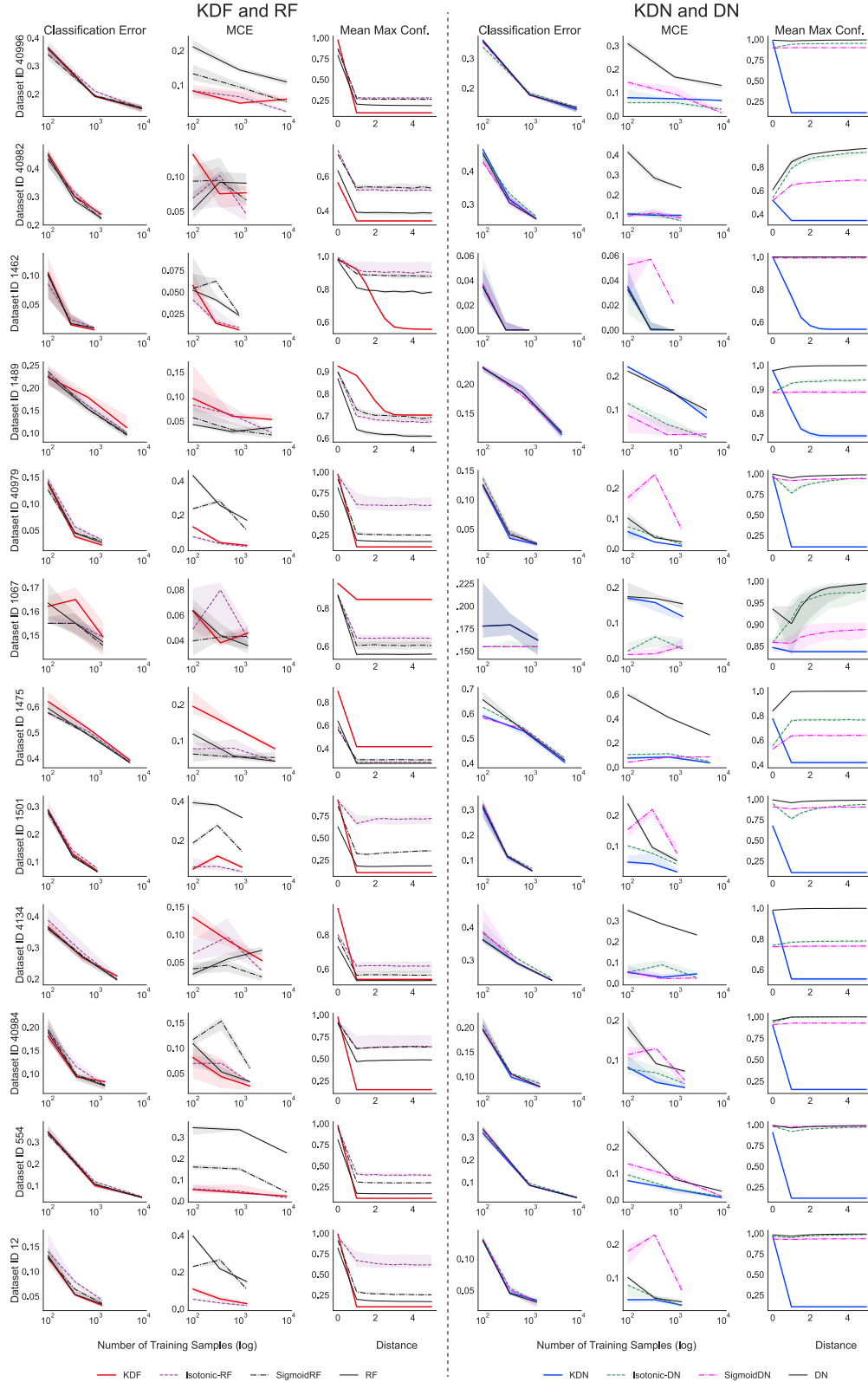


Figure 7: **Extended results on OpenML-CC18 datasets (continued).** *Left:* Performance (classification error, MCE and mean max confidence) of KDF on different Openml-CC18 datasets. *Right:* Performance (classification error, MCE and mean max confidence) of KDN on different Openml-CC18 datasets.

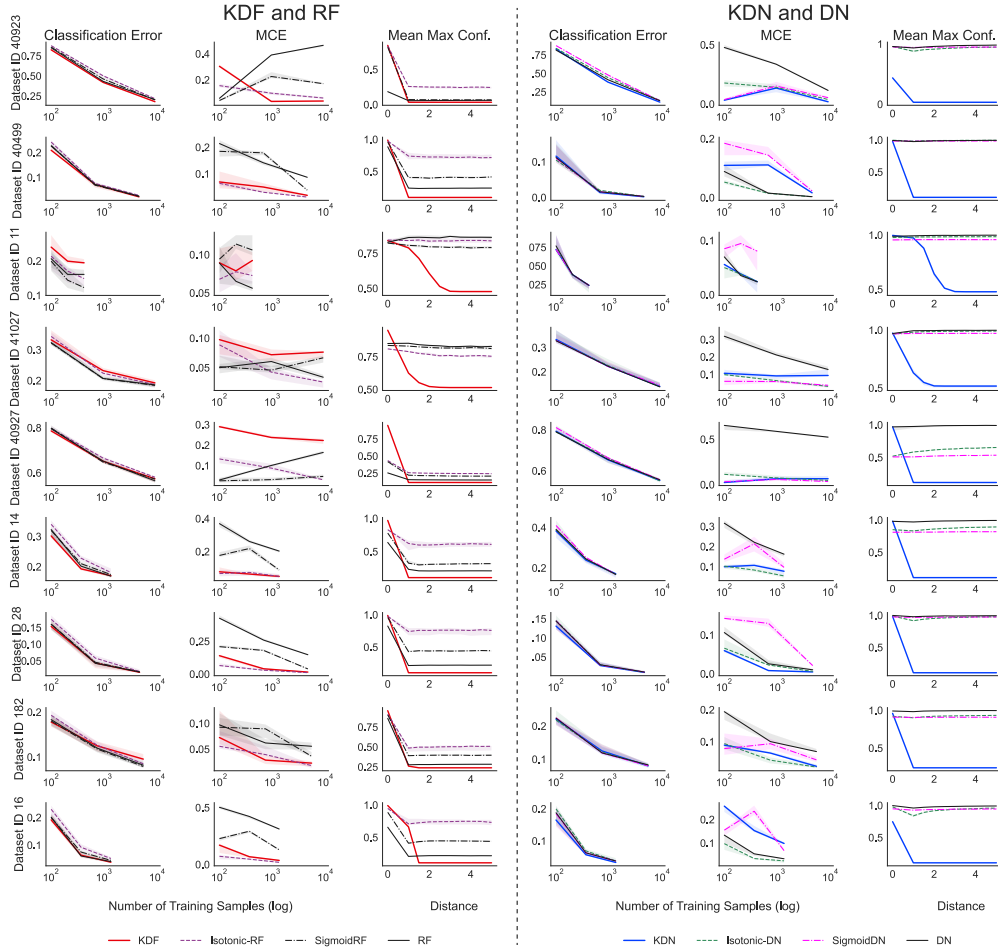


Figure 8: **Extended results on OpenML-CC18 datasets (continued).** *Left:* Performance (classification error, MCE and mean max confidence) of KDF on different Openml-CC18 datasets. *Right:* Performance (classification error, MCE and mean max confidence) of KDN on different Openml-CC18 datasets.